Temperature Estimation and Compositional Mapping Using Spectral Mixture Analysis of Thermal Imaging Spectrometry Data

by Edward F. Collins,[a] Dar A. Roberts,[a] Paul C. Sutton,[b] Chris C. Funk,[a] and Christoph C. Borel [c]

[a] University of California, Santa Barbara, CA 93106

[b] University of Denver, Denver, CO 80208

[c] Los Alamos National Laboratory, MS C323, Los Alamos, NM 87545

ABSTRACT

In the thermal infrared (TIR), a surface emits radiation based on its temperature and emissivity. TIR imaging spectrometry involves extracting temperature, emissivity, and/or surface composition information, which are useful in a wide variety of studies ranging from climatology to land use analyses. A simple technique of temperature emissivity separation (TES) has been developed to separate the effects of emissivity from temperature within the radiance signal recorded by a sensor. This technique can be employed to map the composition and temperature of a surface. Likewise, spectral mixture analysis (SMA) has been successfully applied in this spectral region to discern spectral features and their temperatures. This paper describes an application of TES and SMA that has been employed to characterize the isothermal combinations of thermal radiance features on a sub-pixel basis. This approach, referred to in this paper as a Temperature Emissivity Separation Spectral Mixture Analysis (TESSMA), uses the relationship between a 'virtual cold' endmember fraction and surface temperature to extract image temperature estimates, which are then used to constrain an isothermal unmixing of pixel endmembers. Work presented includes characterizations of synthetically generated temperature-endmember fraction test images, a discussion of methods used to separate temperature and endmember attributions, and a fraction estimate analysis. This paper also demonstrates the temperature dependence of isothermal SMA on accurate temperature estimates, two TESSMA approaches, and their results.

Keywords: spectral mixture analysis, temperature emissivity separation, thermal infrared spectrometry, unmixing

1. INTRODUCTION

TIR imaging spectrometry can be used to retrieve the temperature and emissivity of objects, and has applications in geology,[1] climatology,[2] radiation budget calculations,[3] geophysical process analyses,[4] and atmospheric plume studies.[5] Other applications include surface constituent identification for land use mapping,[6] disaster assessment,[7] and change detection.[8] Before applying TIR imagery to such tasks, it is often important to separate the contributions of temperature and emissivity to thermal radiance spectra.

TES and SMA are two classes of procedures used in TIR spectrometry to separate temperature and emissivity contributions to radiance images. TES involves separating these two constituents using constrained assumptions about the temperature and emissivity contributions to the spectral signature. Spectral mixture modeling,[9] also called SMA,[10] is an established tool for estimating the sub-pixel constituents (endmembers) of a scene using a linear or nonlinear mixing model. SMA is recognized as a method for separating constituents, such as land cover types, and as a method of extracting elemental and mineralogical information.[10]

A virtual cold (VC) endmember approach [11] is an extension of the shade concept from visible/near infrared studies to the TIR. Both original and more recent work in visible/near infrared SMA have taken multiple scattering into account by using a virtual shade endmember, which incorporates multiple scattering by solving for a unique shade endmember such as radiative or canopy shade[12]. This technique may be applied in SMA to reduce non-linearity effects. Likewise, in the TIR spectral region, application of an analogous method uses VC to assist in the definition of the temperature variation within a TIR image.[13] A fundamental difficulty in using this approach, however, is that the temperature-radiance relationship is nonlinear. This nonlinearity produces a surface

Part of the SPIE Conference on Imaging Spectrometry V • Denver, Colorado • July 1999
SPIE Vol. 3753 • 0277-786X/99/$10.00

radiance response which is not separable in terms of temperature and wavelength. [13] One approach that addresses this nonlinearity is the application of an exhaustive analysis using all SMA endmember-temperature combinations. For large projects or large endmember sets, such an approach can be computationally impractical.

Temperature induced nonlinearity in the emitted radiance causes an isothermal SMA to produce errors in endmember fractions when the surface temperature diverges from those of the endmembers used. Although the resulting fractions are not always representative, there is a consistent relationship between the VC endmember fraction and the temperature of isothermal pixels. Various methods of calculating the temperature using this relationship were used, and some of these results are discussed in the following analysis. Using a temperature estimate, endmember fractions may be calculated using a temperature-constrained isothermal SMA approach. Two of these TES and SMA (TESSMA) methods using the VC-temperature relationships are compared, and conclusions drawn. Results appear promising, but further research is required.

2. METHOD

Synthetic images were generated using a simulation of the transmitted radiance of sub-pixel spectral mixtures. These mixed pixel images were then processed using anisothermal SMA. A relationship between pixel temperature and VC endmember fractions was used to generate four temperature estimates. Two of these temperature estimates were used to constrain isothermal SMA of each pixel in the synthetic images. The results of these procedures are then discussed.

2.1. Sensor radiance estimation

Synthetic radiance estimates were generated using MODTRAN[14] simulations. Emissivity spectra from the ASTER spectral library[15] were used to provide a controlled method for testing the approaches used. In order to develop test images and endmember classes, seven spectral signatures (water, green vegetation (GV), non-photosynthetic vegetation (NPV), quartz, sandstone, and two soils) were resampled to 128 bands from 7.8 to 13.5 micrometers. Original emissivity values (Figures 1A and 1B) were combined with MODTRAN runs for a standard continental summer with a winter water vapor profile to represent spectral radiance estimates for a temperature range of 260 to 350 K for a flight at 3 km altitude over a 1 km elevation site in the Southwest United States.

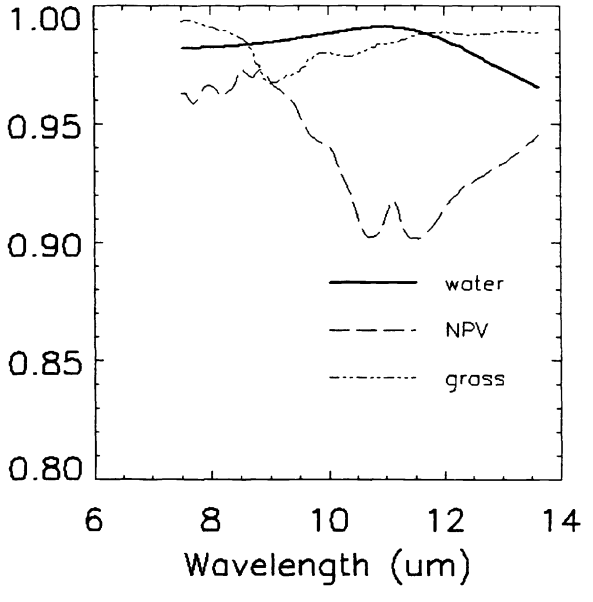

Figure 1A: water, NPV, and grass emissivities

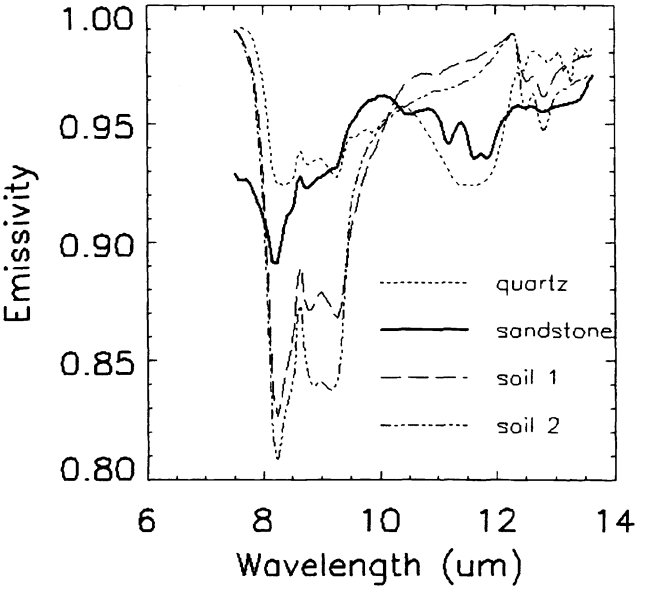

Figure 1B: quartz, sandstone, soil 1, and soil 2 emissivities

Figure 1: Emissivity spectra for eight endmembers used with MODTRAN to develop test images and endmember models.

These emissivities, when used in conjunction with MODTRAN atmospheric modeling, were used to produce sensor radiance estimates at 1 K increments for the site. Each temperature value has a different sensor radiance response, as predicted by Planck, and includes atmospheric transmission, emission, and surface reflectance effects. Figure 2 shows radiance estimates from 260 to 350 K in 10 degree increments, and shows some of the nonlinearity of sensor radiance with temperature. Differences in radiance are smaller at lower temperatures than at higher temperatures. This will have an effect on anisothermal SMA, as discussed later. These sensor radiance estimates were used to generate both the endmember model and synthetic spectral mixture images.

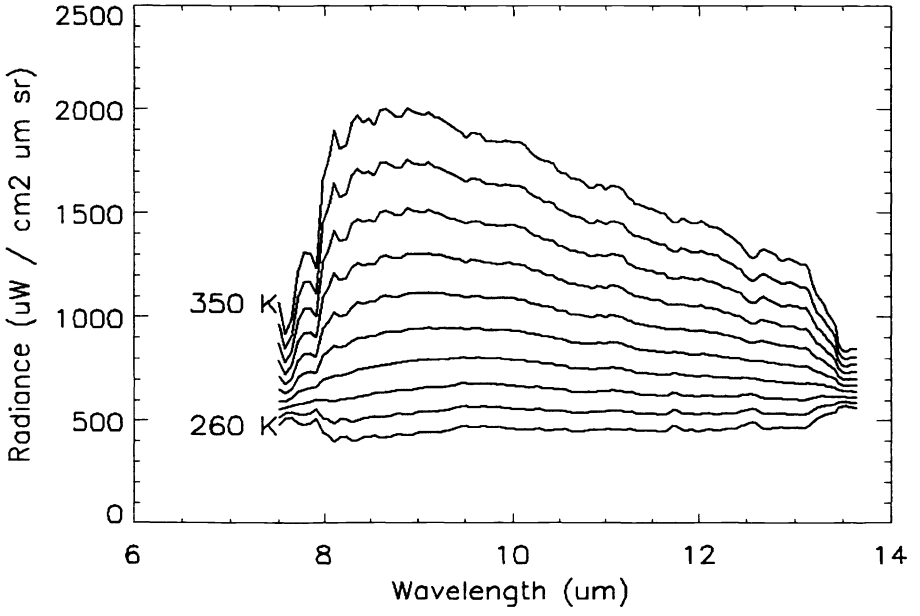

Figure 2: NPV sensor radiance estimates at 10 degree temperature intervals.

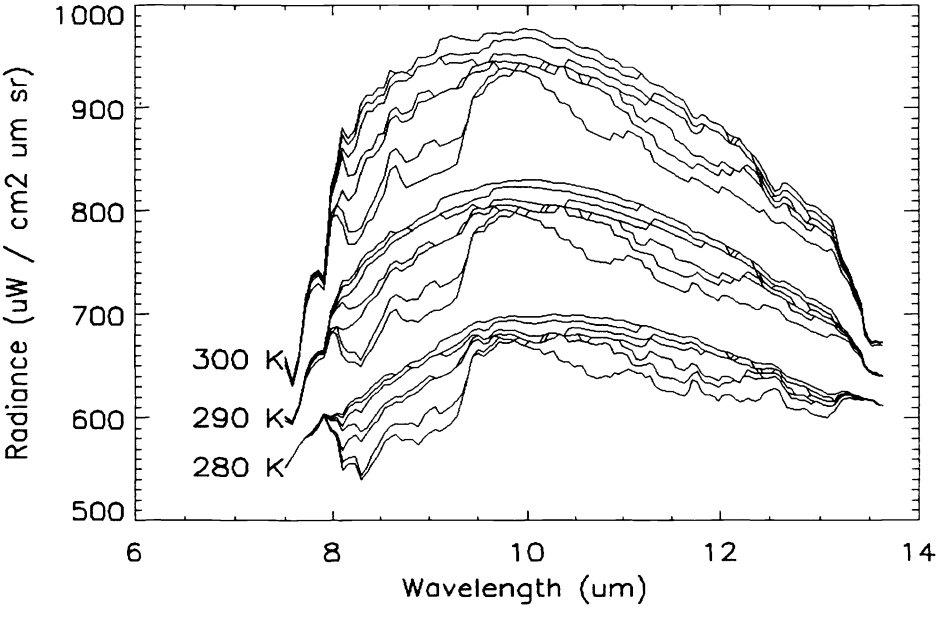

Figure 3: Radiance spectra for the seven model endmembers at three temperatures.

2.2. Spectral endmember model

The spectral endmember model was generated using the radiance estimates. Each class, such as the one shown in Figure 2, has one radiance spectrum, or endmember, for each temperature. Our analysis used endmembers for seven classes (water, GV, NPV, quartz, sandstone and two soils) at temperatures ranging from 280 to 330 K, and one VC endmember, which uses the average spectral emissivity for all 7 classes at 260 K. Figure 3 shows the radiance estimates for these seven classes at three different temperatures; 280, 290, and 300 K.

In this analysis, the same emissivity values and atmospheric simulations were used to generate the SMA endmember model and the synthetic images. This allows for a direct comparison of the unmixing methods under optimal conditions. The majority of the variability in the endmembers is due to the temperature range of the endmember model. However, Figure 3 shows that a recognizable and separable fraction of the effect is generated by the emissivity.

2.3. Synthetic image generation

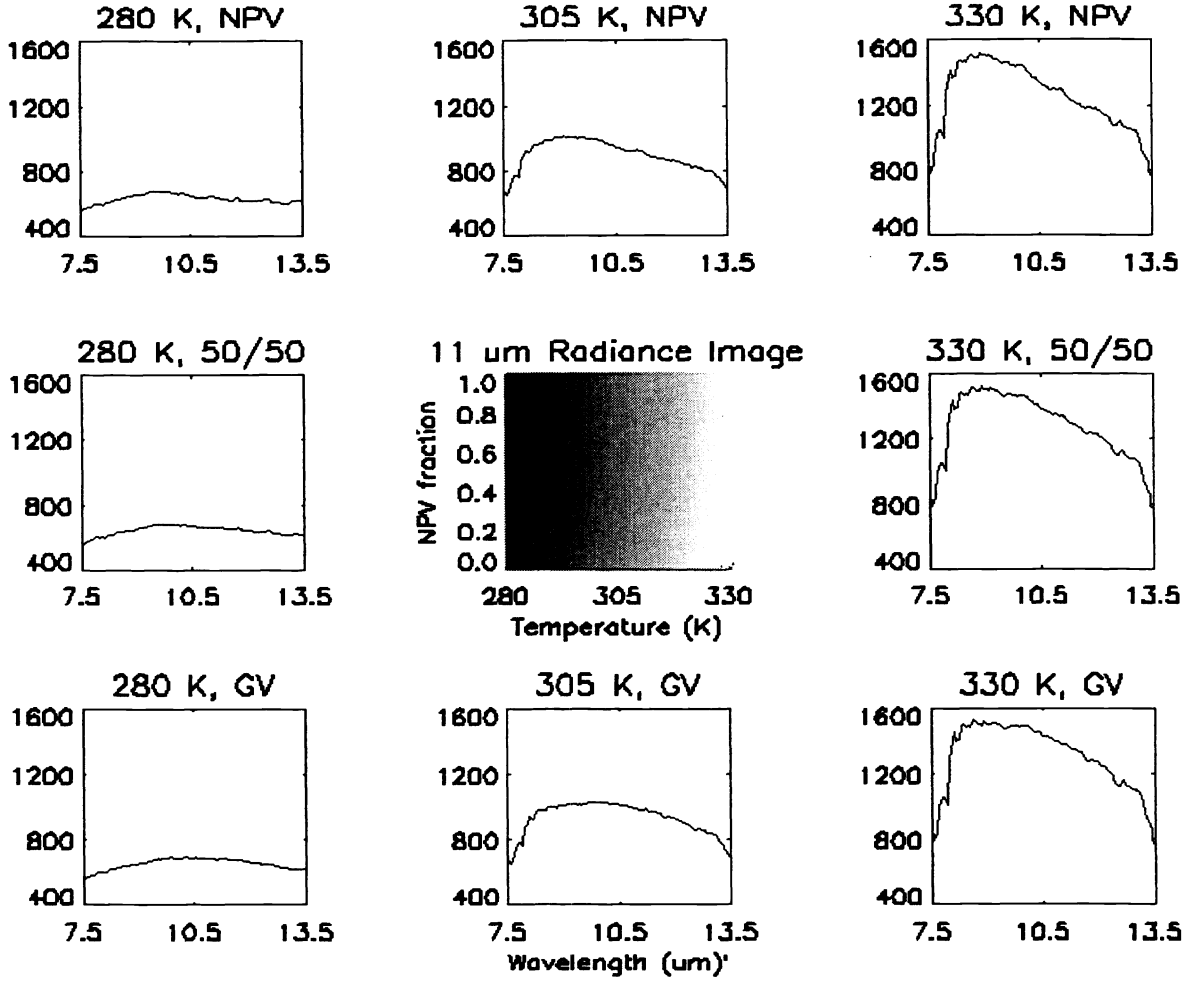

Figure 4: Isothermal two-endmember NPV - GV mixed pixel image and sample spectra from corners and sides of the image. The central image shows the radiance at a particular band, while the graphs around it show the spectral radiance values at several endmember fraction and temperature points in the image. A 50/50 graph represents a sample with equal fractions of NPV and GV.

The image in Figure 4 shows the radiance at 11 um, while the graphs around it show the spectral radiance values at the corners and the middle of the edges of the image. The synthetic image in Figure 4 was derived from a linear interpolation of radiance spectra, illustrated in Figure 2, which were derived from MODTRAN calculations of spectral radiances for the emissivities shown in Figure 1. Images derived in this manner are used as the basis for subsequent analysis and discussion. These temperature and endmember fraction gradient images allow characterization of best case expectations for various unmixing algorithms.

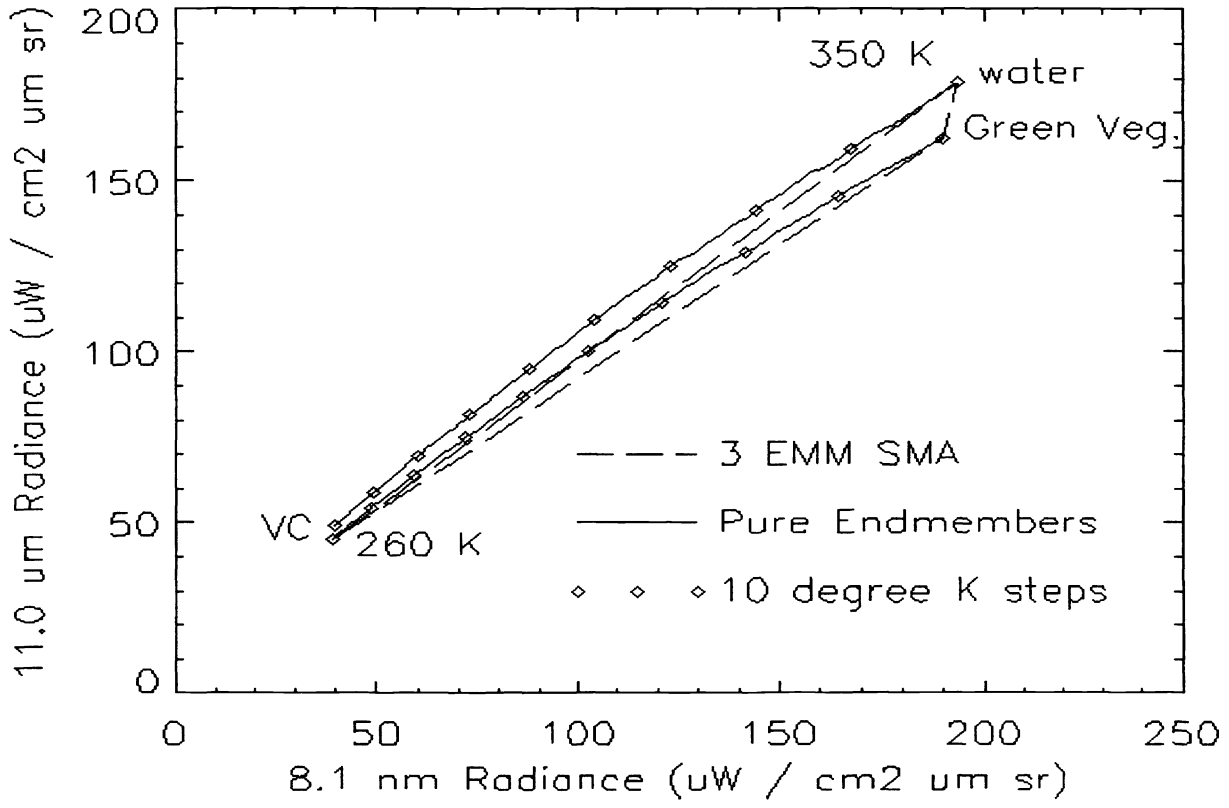

Figure 5: Nonlinearity compared to a SMA model. Band radiances at ten-degree intervals from 260 to 350 K. Actual temperatures lie outside the triangular SMA model boundary, leading to errors in endmember fraction estimates. Nonlinearity is also apparent in the increased distance between 10 K steps (shown as diamonds) with higher temperature along both pure endmember lines.

One of the basic assumptions of SMA is that the resulting image is a linear combination of the fractional contributions of the image constituents, and shade endmembers are often used to reduce nonlinearity effects. One of the added difficulties of a simple SMA approach in the TIR, rather than the visible/near infrared, spectral regime is that anisothermal endmember mixtures are nonlinear. Figure 5 demonstrates this non-linearity. Also inherent in the use of SMA is the assumption that the endmembers define the extreme range for mixtures of their classes and that ideally a mixture of three constituents will lie within a triangle described by endmember vertices. This assumption is illustrated by the dashed triangle in Figure 5 for water, GV, and VC endmembers.

The GV and NPV classes in Figure 5 converge at low temperatures, and an average of the calculated sensor radiances for each band is used to define what is referred to as a VC endmember. The hot endmembers in Figure 5 are 350 K in this example, while the cold endmember is at 260 K. The very narrow triangle shows the regime within which linear mixing would be expected. Many of the pure endmember temperatures fall outside this linear mixture assumption. Applying a partially constrained SMA using these extreme endmembers would yield strong negative and positive (<100% fraction) estimates, which are not representative of the image mixture.

2.4. Temperature look - up table

In SMA, the temperature of isothermal mixtures is consistently reflected in the VC endmember fraction, as seen in Figure 6. This consistent response in the TIR estimation allows recalculation of a more accurate temperature estimate. The solid line in Figure 6 is the mean VC fraction estimate for a 7-class three-endmember model, and temperature estimates may be made using a lookup table based on this mean VC-temperature relationship. The SMA endmember fractions were constrained to sum to 1.0, but individual endmember fractions were not constrained.

Two major approaches were compared. The first approach is a spectral mixture model using two hot temperature combinations of all seven model endmembers and a VC spectrum. Temperature is estimated from the virtual cold fraction using the VC - temperature lookup table. The second approach differs from the first by using a two - endmember average spectral match in place of the three - endmember model using seven classes. In both models, the sum of endmember fractions was constrained to 1.0, while individual endmember fractions were unconstrained. Both of these temperature estimates are subsequently used separately to generate endmember fraction estimates using an isothermal two - endmember model with the same seven spectral classes. The results of these two estimates are compared to assess their success at correctly predicting endmembers and endmember fractions.

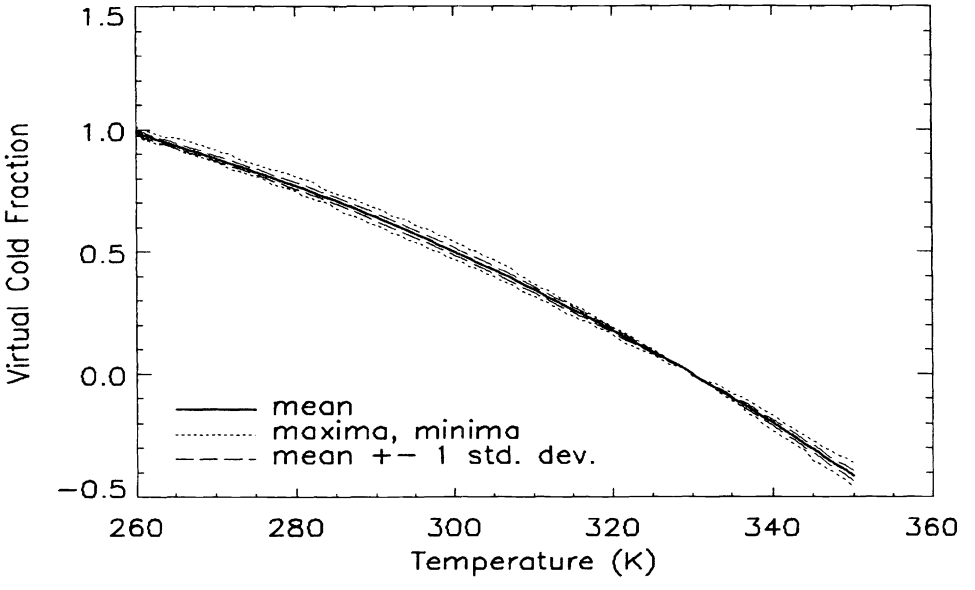

Figure 6: VC fraction as a function of temperature for an isothermal SMA using 7 hot endmember classes at 330 K. The temperature of isothermal endmember mixtures is consistently reflected in the VC endmember fraction.

2.5. Training image

A training image was developed to ensure that the VC-temperature lookup table is representative of the range of image constituents. The temperature endmember image is similar to Figure 4, but incorporated 20 percent fraction interval mixtures for all two endmember combinations possible for 7 endmembers. This image was used to compare the overall temperature accuracy of the various anisothermal models, including the one shown in Figure 6.

2.6. Isothermal unmixing

Isothermal unmixing was applied to individual synthetic images using temperature estimates as constraints to pixel-based unmixing. Two anisothermal SMA were used: a 7 - class three - endmember SMA using hot endmembers at 330 K, and a two - endmember SMA using a 7 class average hot endmember at 330 K. Three synthetic mixture images were processed in this manner: NPV-GV, water-GV and soil2 - GV fraction images. Individual endmember fractions in the isothermal SMA were limited from 0.0 to 1.0, and the sum of their fraction estimates was 1.0.

3. ANALYSIS

3.1. Simple SMA

Anisothermal SMA was found to provide fairly good endmember and fraction estimates near the hot endmember temperature, but became increasingly less accurate at lower temperatures. Figure 7 shows an example of four attempts to unmix the NPV - GV synthetic image shown in Figure 4 using two endmember pairs and VC, and demonstrates this model temperature based effect.

Four spectral mixture models are shown: NPV-GV, water-GV, NPV-soil2, and soil1-soil2. The first row contains plots of the VC-temperature relationship for all four models. The second and third rows contain plots of SMA model vs. actual fractions of the NPV and GV endmembers for 6 temperatures: 330, 320, 310, 300, 290, and 280 K. These values are ordered from top (330 K) to bottom (280 K) in the last row, but are clumped together in the middle row.

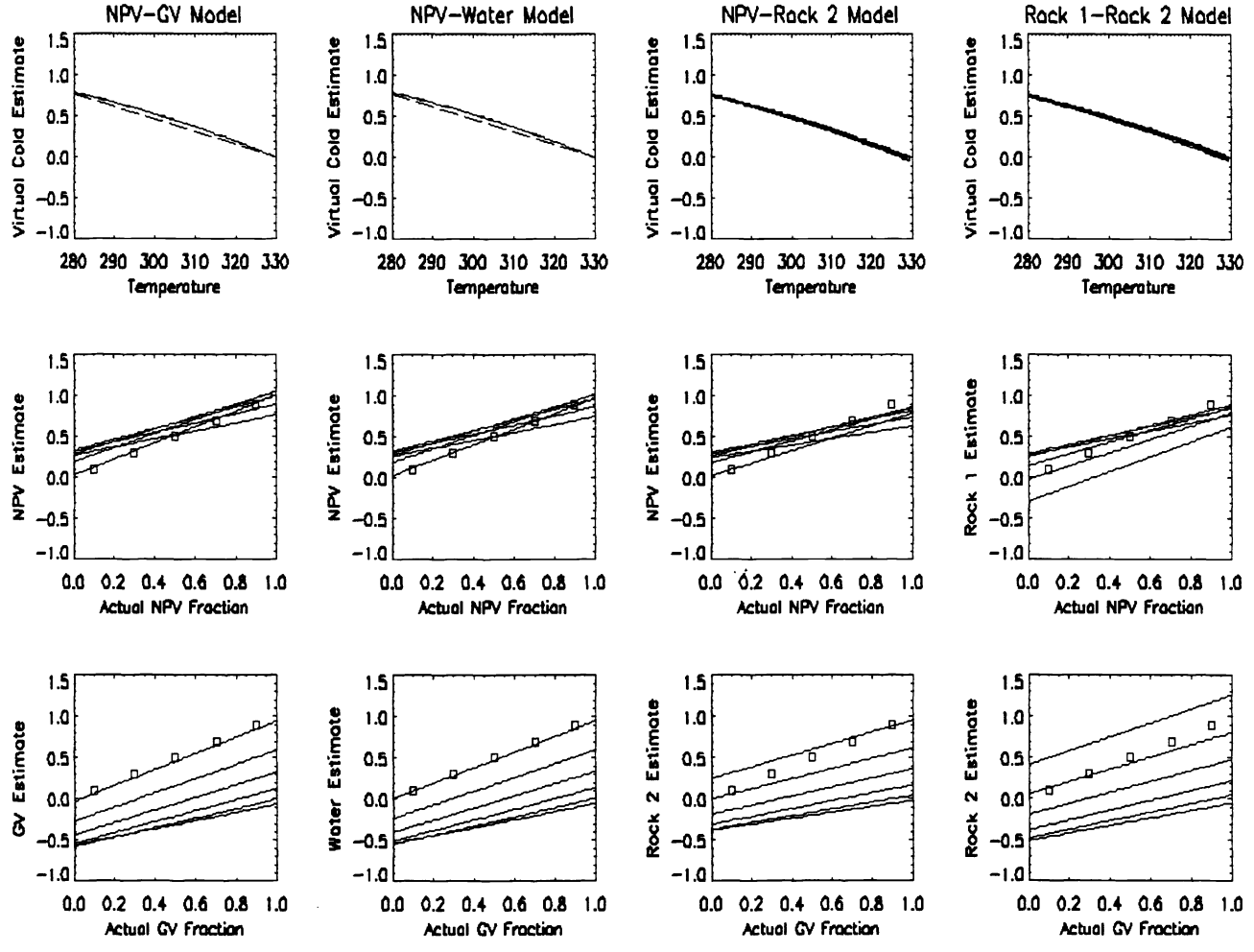

Figure 7: Endmember fraction estimates versus temperature and actual fractions for four models applied to a NPV – GV test image. The top row shows VC - temperature relationships. The middle row shows the relationship between fraction estimates and NPV fractions. The bottom row shows the relationship between fraction estimates and GV fractions.

The first row of Figure 7 shows the VC fraction for all endmember compositional pairs plotted against temperature. The dashed line in the first row represents the expected values for a linear mixture. The relationship between VC endmember fraction and

temperature is consistent. The match with the least variability in this estimate is found in the first column, in which the same endmember model was used to unmix the image.

The relationship between the hot endmember fractions (NPV and GV) and the actual image fraction is more clearly represented by comparing the model and actual fractions at several temperatures. The second and third rows show a comparison of the actual and estimated percentages of NPV and GV. The relationship between these endmember pairs and temperature is less uniform than the VC-temperature relationship, and fraction relationships were drawn for several temperatures to compare actual and predicted endmember fractions.

Each solid line in rows 2 and 3 is a plot of estimated and actual hot endmember fractions for each of the following temperatures; 330, 320, 310, 300, 290, and 280 K. The NPV fraction estimates (shown in the middle row) at these temperatures were clustered, indicating a reduced temperature effect than was found in the GV fraction comparisons. The upper line in the GV fraction comparisons (shown in the lower row) contains the 330 K match, and successively lower matches are ordered below this line. This strong pattern in only one of the fraction estimates indicates that one endmember fraction estimate is less affected by temperature than the other.

The boxes in the lower two rows which contain these plots represent the expected composition match for endmember fractions for hot endmembers at 330 K. The 330 K endmember line should intersect these boxes. Hot endmembers for the 330 K mixture combinations do intersect for the correct (NPV-GV) model and for the nearly correct (NPV-water) model. This implies that fraction estimates for very close attribution mismatches (e.g. water -> GV) may be fairly close to that of the image, even though the attribution is incorrect.

The first column in Figure 7 shows an example in which the model and image endmember pairs match. In this case, the VC - temperature relationship is very consistent for all mixture fractions, and is close to the projected linear mixing assumption shown with a dashed line. The NPV endmember shows a close approximation to the projected endmember fractions for the hot (330 K) mixed pixel case, and a close approximation for the other (320, 310, 290, and 280 K) cases. The GV endmember is also correct for the hot mixed pixels, but diverges from this line for lower temperatures. This is considered to be a consequence of the effect of intermediate temperatures on the isothermal radiance mixture in the image pixel, and the similarity of the GV and VC spectral signatures.

The second column in Figure 7 shows a case in which a close endmember, water, is substituted for GV in the model. Results are similar to that of the NPV-GV model. This is expected because the spectral signatures of water and GV are similar. The third column shows the results of a NPV-sandstone endmember model applied to the same NPV – GV image. In this case, the VC fraction estimate broadened slightly, while the other two-endmember fractions also shifted slightly. The sandstone endmember is sufficiently different from the GV endmember to cause this shift.

The fourth column of Figure 7 shows the results of a quartz-sandstone endmember model used on the same NPV – GV image. This demonstrates that an increased variability in the composition estimates for the two hot endmembers and a similar broadening of the VC fraction estimate can be expected when the selected model endmember diverges significantly from the image endmember. The overall effect of the endmember mismatch is small for the VC endmember fraction, and can be quite pronounced for both hot endmember fractions. The larger overall mismatch is attributed to the dissimilarity of the image and model endmembers.

In summary, Figure 7 shows that the VC-temperature relationship is consistent. Furthermore, this relationship is not as sensitive to the selection of incorrect endmembers. However, the other actual endmember fraction estimates can vary considerably from the original class estimates when the model and image endmember temperatures diverge. These values can be off by as much as 100%. Finally, the fraction estimates are not uniform in their variability with temperature, indicating that a simple adjustment, such as dividing by (1 - %VC), will not provide a correction of the fraction estimates.

3.2. Temperature estimation

The VC endmember fraction – temperature lookup table (Figure 6), was used as a means of estimating temperature in mixed TIR spectra. The average VC fraction – temperature relationship varies both with the endmember model used and the temperatures of the hot and cold endmembers. As a result, the accuracy of their model temperature estimates may also vary.

To assess the utility of VC as a means for estimating temperature and the impact of model selection on temperature estimate errors,four models were compared; three multiple endmember models using hot endmembers of 350, 330, and 310 K, and one two-endmember model using a 7-endmember average at 330 K. Figure 8 contains temperature error statistics for these models, and shows the mean error (solid line) for each method. Maximum and minimum error values are shown as crosses (+), and estimates of one standard deviation from the mean are shown as dashed lines.

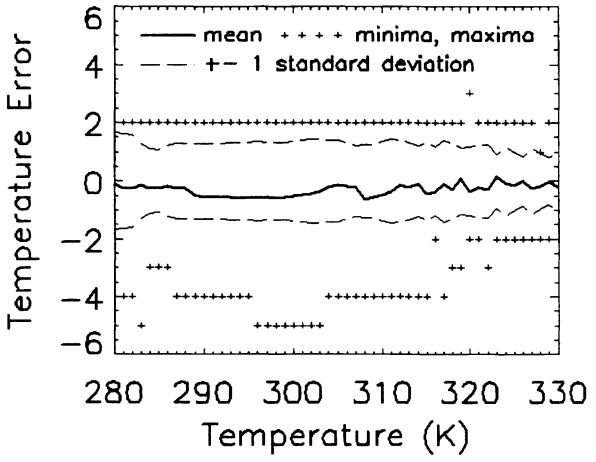

Figure 8A: Seven - Class Hot 3 EMM

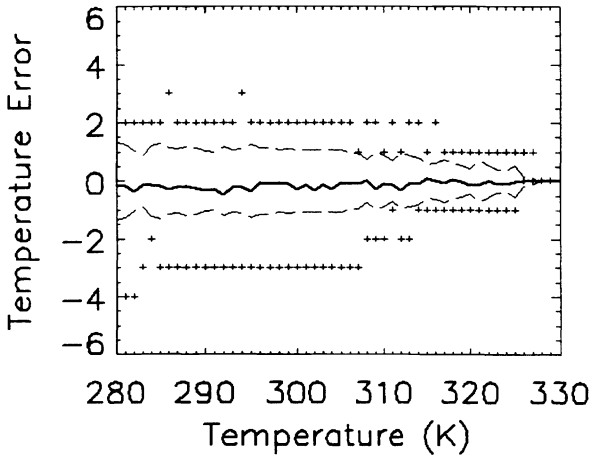

Figure 8B: Seven - Class Warm 3 EMM

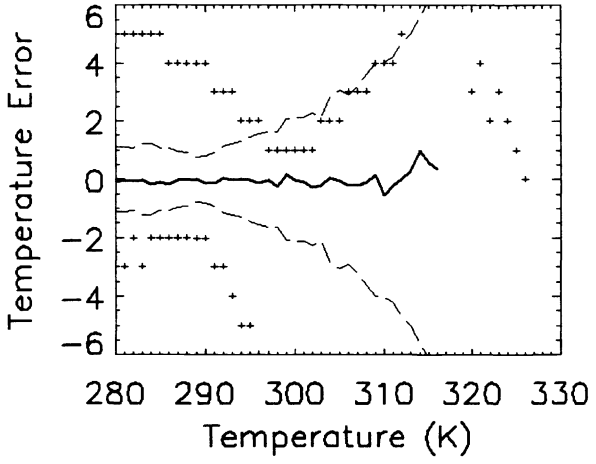

Figure 8C: Seven - Class Midrange 3EMM

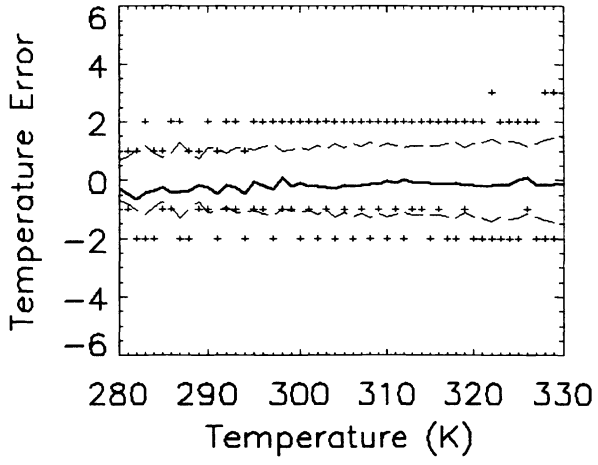

Figure 8D: Class Average 2EMM

Figure 8: Error statistics for four temperature models. Models A, B, and C are three-endmember models using hot endmembers of 350, 330, and 310 K, and D is a two-endmember model using a 7-endmember average at 330 K. The mean errors are shown in solid lines, maximum and minimum error values are shown as crosses (+), and estimates of one standard deviation from the mean are shown as dashed lines.

In Figure 8A, a three - endmember model with a 350 K hot endmembers produced a temperature error range of +2 to -5 K (Figure 8A). This large temperature error reduces the predictive value of this model. Accuracy increases as mixed pixel temperatures approach that of the hot endmembers. Using 330 K hot endmembers, (Figure 8B), produced similar results, with a temperature error range of +3 to -4 K. However, between 315 and 330 K, the error range was +1 to -1 K or less. In addition, the standard deviation for this 330 K endmember model was also lower.

A 310 K hot endmember was tested with the expectation that it would improve the temperature estimation accuracy in the middle of the image. Instead, Figure 8C shows a decrease in accuracy. There may be a minimum distance between endmember temperatures below which the temperature - VC relationship breaks down. The lowest temperature error extremes were observed in the final case using a two - endmember model and an average hot endmember at 330 K (Figure 8D). This test shows a temperature estimate error range of +3 to -2 K, with most extreme values between +2 and -2 K. This model has the advantage of reduced temperature error extremes, when compared to be warm three-endmember model in Figure 8B, but has an overall larger standard deviation. The two most promising models, 330 K hot endmember model (Figure 8B) and the average hot endmember model (Figure 8D), were compared to show the overall effects of temperature errors on the endmember estimation.

3.3. Perfect unmixing using isothermal SMA

Figure 9 Shows the results of unmixing endmembers using an ideal temperature estimate and floating point radiance images. Each of the three images, (NPV-GV, Water-GV, and Soil2-GV) has been isothermally unmixed using the correct temperatures of each pixel. Each of the columns contains fraction estimates for each of the images, with light shades representing high fractions, and dark shades representing low fractions. For this ideal temperature estimate, the only fraction estimates are the ones in the actual images, and they are correct.

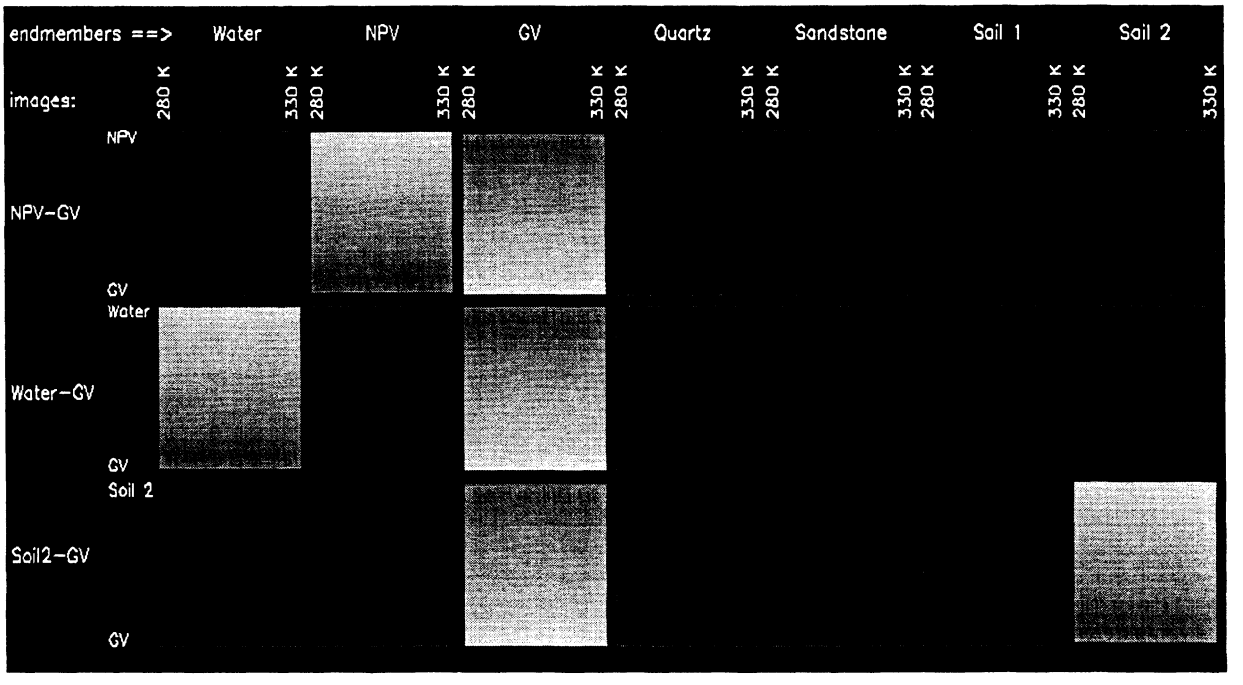

Figure 9: Endmember fraction estimates for three mixed pixel images (NPV-GV, Water-GV, and Soil2-GV) using isothermal unmixing with correct temperature values. Higher fraction estimates are shown in lighter tones, and lower estimates are shown in darker tones.

3.4. Temperature estimation error effects on isothermal SMA

It is expected that as the temperature estimates worsen, both the endmember attribution and the fraction estimate accuracies are reduced, as is illustrated in Figure 10. In this figure, an integer NPV-GV fraction radiance image was isothermally unmixed five times using SMA. The middle column shows an isothermal unmixing estimate using the actual temperatures used to generate the image. In this case, approximately correct endmember fractions are estimated. The top row, using a temperature estimate 2 degrees higher than the actual temperature, has greatly reduced attribution and fraction accuracies. The second row contains an isothermal unmixing with a temperature estimate one degree higher than that of the actual image, and the accuracies are closer to the ideal case than a 2 K temperature over-estimate.

The lowest two rows in Figure 10 show underestimation of 1 and 2 K. The 1K underestimate has similar attribution and fraction errors to that of a 1K overestimate, although individual estimate accuracy patterns vary considerably. Likewise, a 2K underestimate would yield similar total attribution and fraction errors, and very different patterns in the individual estimates. Both 1 and 2K overestimate fraction errors for both classes in this particular (NPV-GV) case were assigned to the water endmember, while errors in the 1 and 2K underestimate for this particular case were assigned to other endmembers.

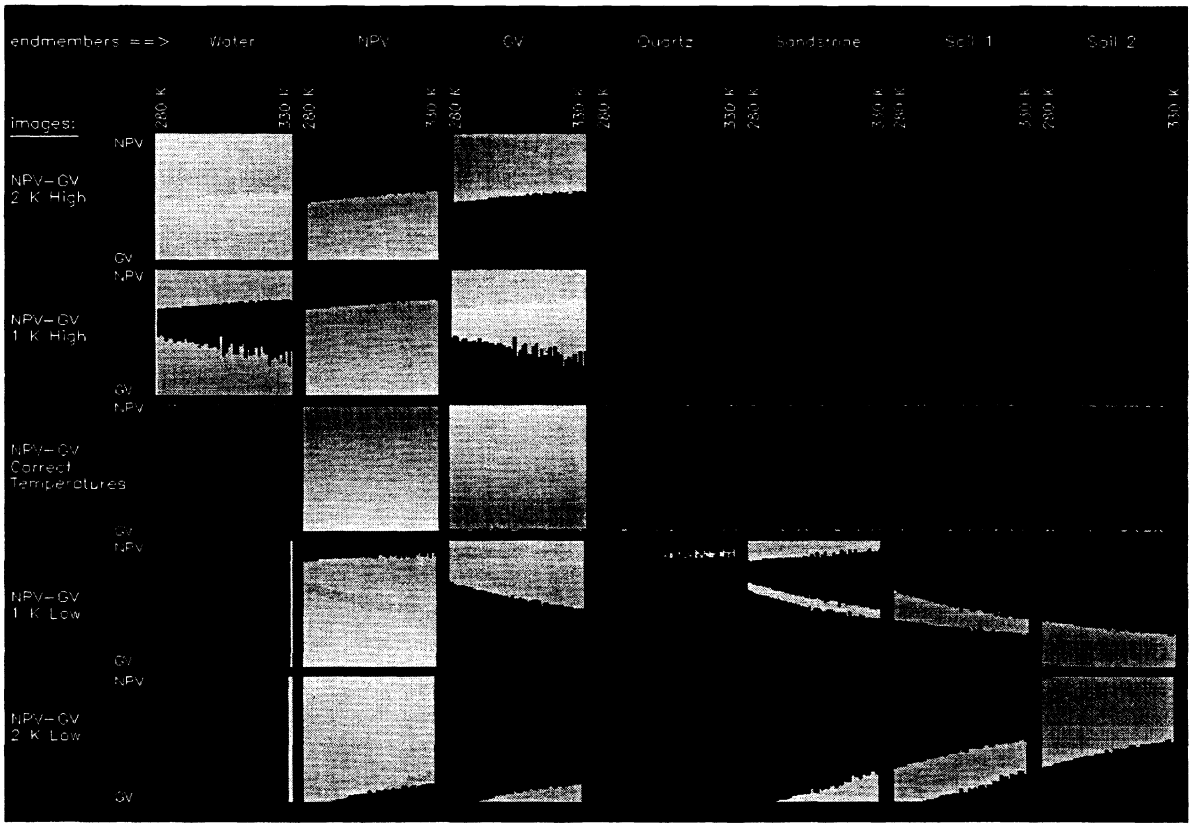

Figure 10: Isothermal unmixing endmember fraction estimates for one mixed pixel image (NPV-GV) using 5 temperatures. The middle set of fraction estimates (row 3) uses the correct temperature, and has correct endmember and fraction estimates. The temperature estimates 1 K warmer (row 2) and 2 K warmer (row 1) are more inaccurate than fraction estimates for temperature underestimation cases -1 K (row 4) and -2 K (row 5).

3.5. Isothermal SMA using anisothermal SMA generated temperature estimates

The temperature estimates were then used as inputs to an isothermal SMA application using the three image pairs; NPV - GV, water - GV, and GV - soil 2. Figure 11 shows the results of this procedure using the seven -class warm three - endmember model temperature estimates shown in Figure 6 and Figure 8B. The correct fraction estimates are available in Figure 9, for comparison. The first row shows the fraction estimates for each member in the isothermal unmixing of the NPV - GV image. The correct unmixing for the NPV - GV image is visible on the right hand side of the NPV and the GV fraction estimates. In this approximately 6 degree temperature span from 325 to 330 K, the temperature estimates are mostly correct, and both endmember attribution and fraction estimates are mostly correct. Outside this range, the GV and water endmembers are likely to be more confused. For higher NPV fractions, the majority of the fraction estimates are incorrectly attributed to water. Other incorrect attributions also show up in the endmembers in the right of the figure.

The second row of Figure 11 contains fraction estimates for the water - GV image. Like the previous image fraction estimate, the temperature range of approximately 325 to 330 K, on the right hand side of the water and GV fraction estimates, is mostly correct. Beyond this range, approximately half of the fraction estimates are incorrect.

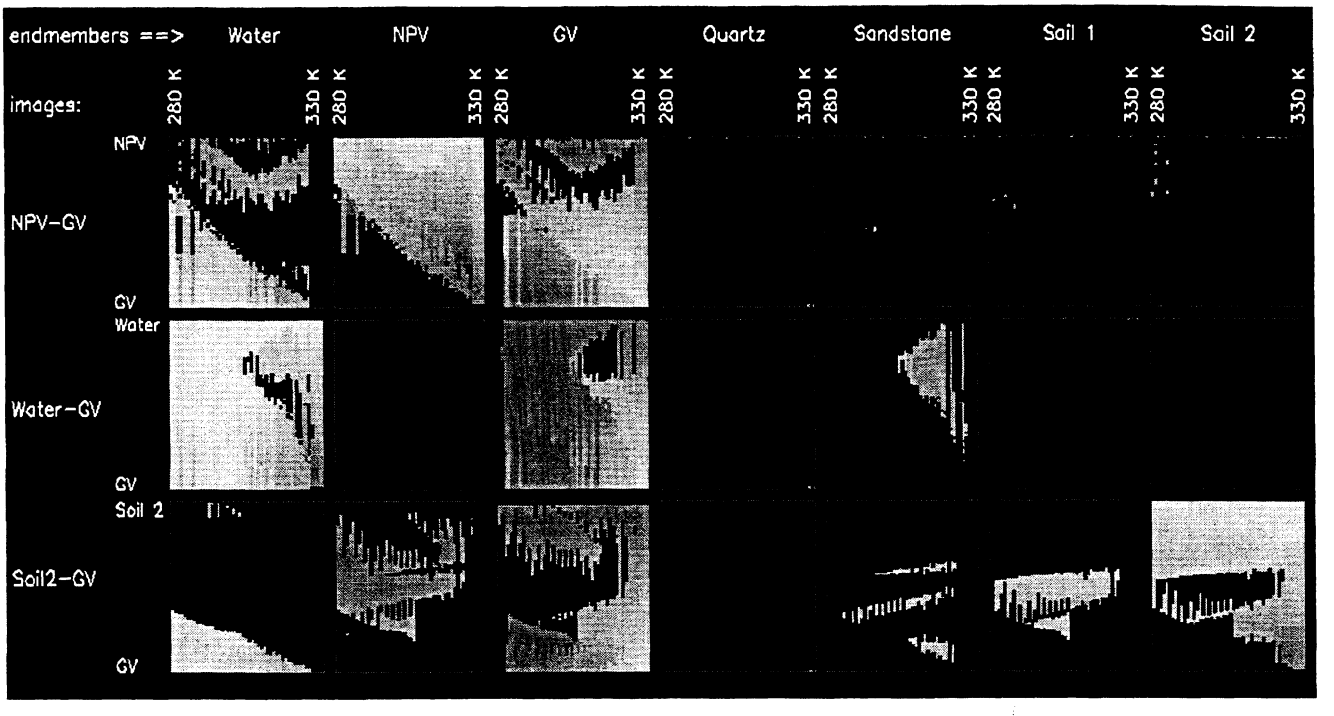

Figure 11: Isothermal unmixing fraction estimates for three test images using a 7-class three-endmember model temperature estimate. The three rows correspond to the test images. The seven columns represent an endmember estimate for each of the three images. An ideal match for these images may be seen in Figure 9.

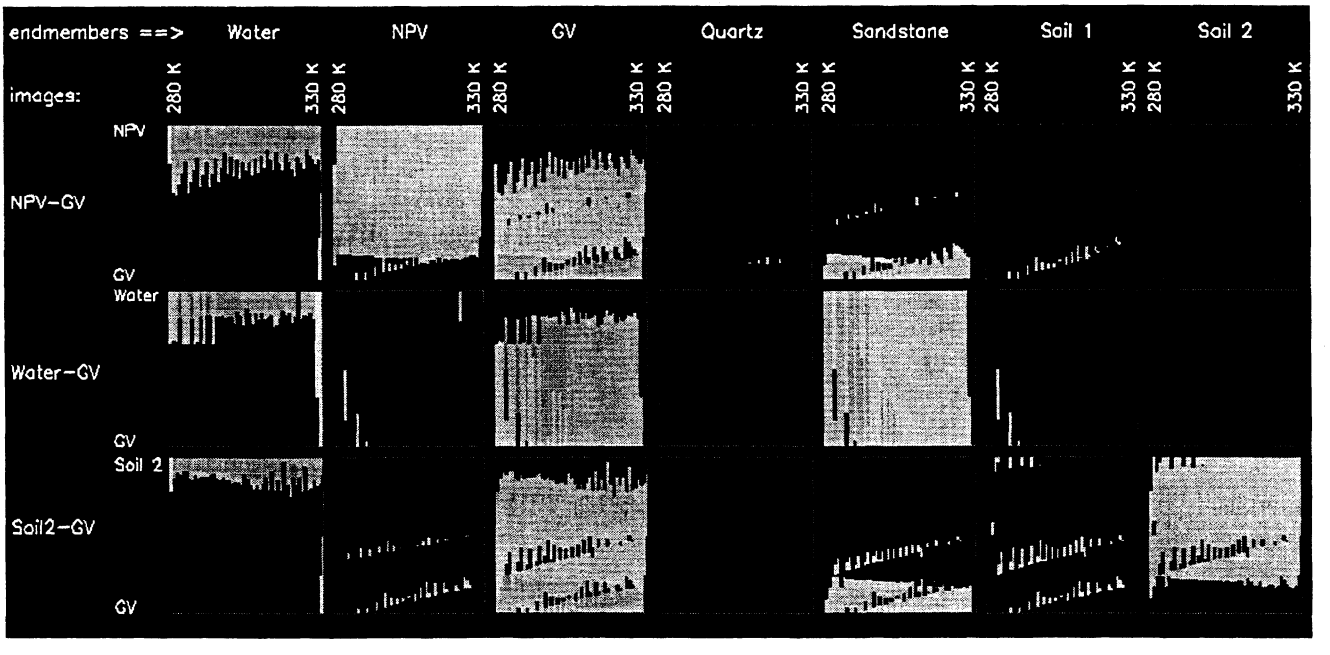

Figure 12: Isothermal unmixing fraction estimates for three images using an average emissivity, 330 K three - endmember model temperature estimate. The three rows correspond to three test images. The seven columns show endmember fraction estimates for each of the three images. Figure 9 contains an ideal image match.

Row three of Figure 11 contains fraction estimates for an isothermal unmixing of a GV - soil 2 image. As in the two previous images, the higher temperature estimates, from approximately 323 to 330 K, are mostly correct. In this case, the soil 2 endmember fraction is approximately half correct. However, other fraction estimates contain considerable errors.

Figure 12 contains the same image class estimates for isothermal unmixing using a temperature estimate derived from the warm two - endmember model. Temperature error statistics for this model are shown in Figure 8D. The first column of Figure 12 shows the class fraction estimates for an NPV - GV image. This image has fairly good class attributions, but poor class fraction estimates. Row 2, containing the water - GV image, shows a strong misclassification of grass or water endmembers with sandstone. This is probably due to temperature estimation errors, which are caused by the difference between the high emissivity water and GV spectra and the derived average spectrum. Likewise, Figure 12 shows a good recognition of the GV and soil2 spectra, but only a fair estimate of the fractions of these constituents.

4. DISCUSSION

Both gray body and multiple hot endmember approaches using a VC look up table produced promising results. Temperature estimation using an average emissivity approach yielded a lower maximum error, while a three - endmember approach yielded a lower root mean squared temperature error. The two approaches yielded similar overall fractional errors, although the multiple endmember approach produces better results for hot endmembers, and the average emissivity approach produces better results for colder temperatures.

There are several basic assumptions used in this model: linear mixing, isothermal mixing, perfect modeling of atmospheric radiation transfer, no sensor noise, and endmember sufficiency. However, this approach allows models to be compared within the constraints of those basic assumptions. A logical next step is the characterization and inclusion of these conditions, and a reassessment of projected temperature, endmember attribution, and fractional composition accuracies.

In general, nonlinearity remains an issue with SMA applications, and this problem is exacerbated in the TIR spectral region. An exhaustive approach should yield an adequate solution, but it may be computationally expensive. The TESSMA approach that we have demonstrated provides a quicker alternative.

Applying greater temperature resolution might bring the temperature error down somewhat, but other TES applications have already reported greater accuracies. Possible avenues of future research include using one or more of these TES applications as a front end to the isothermal SMA approach described previously. Other work will include acquiring an increased understanding of atmospheric, endmember description, and sensor constraints on temperature, endmember selection, and endmember fraction accuracy.

The separation of temperature and endmember fraction estimation allows a much more independent choice of methods for each procedure. The best temperature estimation method may then be used to guide a single temperature SMA solution, as demonstrated here. An iterative approach may be used, which should close to a (usually) optimal temperature and endmember fraction estimate. The temperature estimate may be used as a prelude to other mixture analysis techniques. Thus, either or both of the TES and SMA approaches may be replaced to produce better TESSMA algorithms. Furthermore, the SMA algorithm may be used on either radiance or TES generated emissivity estimates.

An iterative, constrained temperature SMA procedure may also produce better temperature and endmember fraction matches. Such approaches have characteristically produced more accurate overall estimates. The excellent temperature estimation in the 315 to 330 K temperature range in Figure 8 B. yields further support to this idea.

A major constraint of TESSMA is the assumption of isothermal mixing. In general, this occurs only twice a day. At other times, fractional endmembers such as soil and vegetation may have different heating and cooling rates, as well as equilibrium temperatures. During daylight hours, shading effects may also compound this difficulty. After constraints to isothermal unmixing using these methods are well understood, techniques for endmember constrained anisothermal unmixing may be required. Such work is predicated on the assumption that accurate endmember assignments have been established using these or other (e.g. visible/near infrared) spectra.

5. CONCLUSIONS

The anisothermal SMA appears to yield good fraction estimates at temperatures near the hot endmember pair, but exhibits increasing errors in endmember attribution and fraction estimates at cooler temperatures. Using a VC fraction and temperature lookup table, satisfactory image temperature estimates were obtained using a three - endmember anisothermal SMA. This approach yielded maximum temperature estimate errors from 0 to 3 K, with errors increasing with distance from the hot endmember pair. The temperature estimate may then be used to isothermally unmix the original radiance image. The most promising temperature-VC relationship, a three - endmember model using VC and two endmembers at the temperature of the upper limit of the synthetic image range, produced good temperature and fraction estimates for the approximately 5-7 degrees adjacent to the hot endmembers. Beyond this range, temperature inaccuracies reduce endmember attribution and fraction accuracies. Future research into this approach using a more accurate TES method should yield good fraction estimates over a broader range of temperatures.

ACKNOWLEDGMENTS

Research funding was provided by a University of California Directed Research and Development grant. Special thanks are extended to Siegfried A Gerstl, at Los Alamos National Laboratories, John Estes, University of California Santa Barbara, and Carrie Cates, University of California Santa Barbara, for their support. ASTER library spectra were provided through the courtesy of the Jet Propulsion Laboratory, California Institute of Technology, Pasadena, California.

REFERENCES:

1. A. R. Gillespie, "Spectral Mixture Analysis of Multispectral Thermal Infrared Images" *Remote Sensing of the Environment,* **42**, pp. 137-145, 1992

2. C. Ottle, M. Stoll, "Effect of Atmospheric Absorption and Surface Emissivity on the Determination of Land Surface Temperature from Infrared Sunlight Data", *International Journal of Remote Sensing*, **14:10**, pp. 2025-2037, 1993

3. M. C. Anderson, J. M. Norman, G. R. Diak, W. P. Kustas, J. R. Mecikalski, " A Two - Source Time - Integrated Model for Estimating Surface Fluxes Using Thermal Infrared Remote Sensing", *Remote Sensing of the Environment*, **60**, pp. 195 - 216, 1997

4. V. J. Realmuto, K. Hon, A. B. Khale, E. Abbott, D. C. Pieri, " Multispectral Thermal Infrared Mapping of the 1 October 1988 Kupaianaha Flow Field, Kilauea, Hawaii", *Bulletin of Volcanology*, **55**, pp. 33 - 44, 1992

5. V. J. Realmuto, A. J. Sutton, T. Elias, "Multispectral Thermal Infrared Mapping of Sulfur Dioxide Plumes: A Case Study from the East Rift Zone of Kilauea Volcano, Hawaii", *Journal of Geophysical Research*, **102: B7**, pp.15057 - 15072, 1997

6. T. J. Schmuggee, F. Becker, Z. L. Li, "Spectral Emissivity Variations Observed in Airborne Surface Temperature Measurements", *Remote Sensing of the Environment*, **35**, pp. 95 - 104, 1991

7. F. G. Sadowski, S. J. Covington, " *Processing and Analysis of Commercial Satellite Image Data of the Nuclear Accident Near Chernobyl, U.S.S.R.*", U.S. Geological Survey Bulletin 1785, Washington, D.C., 1987

8. V. J. Realmuto, K. Hon, A. B. Khale, E. A. Abbott, D. C. Pieri, " Multispectral Thermal Infrared Mapping of the 1 October 1988 Kupaianaha Flow Field, Kilauea Volcano, Hawaii", *Bulletin of Volcanology*, **55**, pp. 33 - 44, 1992

9. J. B. Adams, M. O. Smith, P. E. Johnson, " Spectral Mixture Modeling: A New Analysis of Rock and Soil Types at the Viking Lander 1 Site", Journal of Geophysical Research, **91: B8**, pp. 8098 - 8112, 1986

10. J. B. Adams, M. O. Smith, A. R. Gillespie, "Imaging Spectroscopy: Interpretation Based on Spectral Mixture Analysis", Remote Geochemical Analysis: Elemental and Mineralogical Composition, C. M. Pieters, P. A. J. Englert, eds., pp. 145 - 166, 1993

11. A. R. Gillespie, "Spectral Mixture Analysis of Multispectral Thermal Infrared Images" *Remote Sensing of the Environment,* **42**, pp. 137-145, 1992

12. D. A. Roberts, M. O. Smith, J. B. Adams, "Green Vegetation, Nonphotosynthetic Vegetation and Soils in AVIRIS Data", Remote Sensing of Environment, **44**, pp. 255:269,1993

13.A. R. Gillespie, "Spectral Mixture Analysis of Multispectral Thermal Infrared Images" *Remote Sensing of the Environment,* **42**, pp. 137-145, 1992

14. Berk, L.S. Bernstein, and D.C. Robertson, *MODTRAN: A Moderate Resolution Model for LOWTRAN 7*, Air Force Geophysics Laboratory Technical Report GL-TR-89-0122, Hanscom AFB, MA.

15. S. J. Hook, et al., Spectral Library, Jet Propulsion Laboratory, **http://speclib.jpl.nasa.gov, July 2, 1999**

Correspondence: Email: edward@geog.ucsb.edu; Telephone: 805-893-8116 Fax: 805-893-2578